Coexistence of odd-parity and even-parity order parameters in the multipole order phase of the spin-orbit coupled metal $Cd_2Re_2O_7$

Y. Matsubayashi,[1,*] K. Sugii,[1] D. Hirai,[1] Z. Hiroi,[1] T. Hasegawa,[2] S. Sugiura,[3] H. T. Hirose,[3] T. Terashima,[3] and S. Uji[3,*,†]

[1]*Institute for Solid State Physics, University of Tokyo, Kashiwa, Chiba 277–8581, Japan*
[2]*Graduate School of Integrated Arts and Sciences, Hiroshima University, Higashi-Hiroshima, Hiroshima 739–8521, Japan*
[3]*National Institute for Materials Science, Tsukuba, Ibaraki 305-0003, Japan*

(Received 6 August 2019; revised manuscript received 1 April 2020; accepted 27 April 2020; published 19 May 2020)

Magnetic torque measurements have been performed to investigate the phase transitions of the metallic pyrochlore compound $Cd_2Re_2O_7$, in which a spin-orbit (SO) interaction leads to unique multipole orders associated with an inversion symmetry breaking. We find that the magnetic torque signals with a fourfold symmetry ($\tau_4 \propto H^4$) as well as a twofold symmetry ($\tau_2 \propto H^2$) are significantly enhanced at low temperatures below a structural phase transition temperature (∼200 K). The analyses of the torque curve symmetries show that the τ_4 term arises from an even-parity order parameter (OP) with the irreducible representation E_g, whereas the τ_2 term from an odd-parity OP with E_u, T_{1u} or T_{2u}. The parity mixing of the primary OPs shows a peculiar phase transition in the SO coupled $Cd_2Re_2O_7$. The coexistence of the two OPs provides important insights into the origin of the multipole orders induced by the SO interaction.

DOI: 10.1103/PhysRevB.101.205133

I. INTRODUCTION

The metallic pyrochlore $Cd_2Re_2O_7$ has attracted much attention because of the peculiar symmetry breaking associated with multipole orders due to the strong spin-orbit (SO) coupling and electron correlations [1–5]. The Re^{+5} ion in $Cd_2Re_2O_7$ has two *5d* electrons, whose orbitals mainly form the conduction bands [6]. At $T_{s1} \sim 200$ K, a second-order phase transition takes place [Fig. 1(a)], where the symmetry is reduced from a centrosymmetric cubic structure (phase I: space group $Fd\bar{3}m$) to a noncentrosymmetric tetragonal structure (phase II: $I\bar{4}m2$) [Fig. 1(b)] [1]. This transition is associated with a phonon freezing with the irreducible representation (IR) E_u, dominated by the O ion displacements [7], and is discussed in the framework of the Landau theory with E_u order parameters (OPs) $\boldsymbol{\eta}$ [8–10]. At T_{s1}, a drastic reduction of the density of states [11–15] in spite of very small lattice deformations (for instance, only ∼0.005 Å for the Re-O distance) [1,2] suggests an electronic origin. This transition is discussed in terms of Fermi surface instabilities induced by a SO coupling, which lead to multipolar phases associated with an inversion symmetry breaking [16]. As temperature further decreases, $Cd_2Re_2O_7$ undergoes a first-order phase transition to another tetragonal phase (phase III: $I4_122$) at ∼120 K (T_{s2}) [1]. Recent quantum oscillation measurements in phase III clearly demonstrate coherent transport of the *5d* electrons and the presence of spin-split bands by the SO coupling [6].

Measurements of second harmonic generation (SHG) suggest that phase II has a multipolar nematic order induced by the SO coupling [3,4]. A significant feature is the presence of multiple OPs, two primary OPs with T_{2u} and T_{1g}, and a secondary OP with E_u. Symmetry analyses of the SHG data give a different picture, the presence of two primary OPs with A_{2g} (magnetic octupole) and E_u (magnetic quadrupole), and a secondary OP with E_u (axial toroidal quadrupole) [17]. Although multipole orders induced by the SO coupling [16] are intriguing, the highly controversial issue of the OP symmetries in $Cd_2Re_2O_7$ prevents from the detailed understanding of the transitions. The main reason is that SHG measurements provide insufficient information on the OP symmetries since they are sensitive only to odd-parity OPs but blind to even parity OPs. Therefore, complementary techniques sensitive to even-parity OPs are highly required.

To further investigate the phase transitions induced by the SO coupling in $Cd_2Re_2O_7$, we have measured magnetic torque. The magnetic torque is given by $\boldsymbol{\tau} = \mu_0 \boldsymbol{M} \times \boldsymbol{H} = -\partial F/\partial\theta$, where $\boldsymbol{M}$ and $\boldsymbol{H}$ are the magnetization and magnetic field, respectively, μ_0 is the permeability of vacuum, F is the free energy, and θ is the field angle from a major crystal axis. Since the metallic $Cd_2Re_2O_7$ has no local moments, the magnetization is dominated by the Pauli paramagnetism and orbital magnetism of the itinerant *5d* electrons. In contrast to the SHG measurements, the toque is sensitive to even-parity OPs. We demonstrate that the torque measurement is a powerful tool to investigate OP symmetries of phase transitions.

II. METHODS

The magnetic torque is measured by a piezo-microcantilever technique [18]. The cantilever chip is composed of an atomic force microscope cantilever and a reference lever [Fig. 2]. A single crystal is attached to the

*These authors contributed equally to this work.
†Corresponding author: Shinya.UJI@nims.go.jp

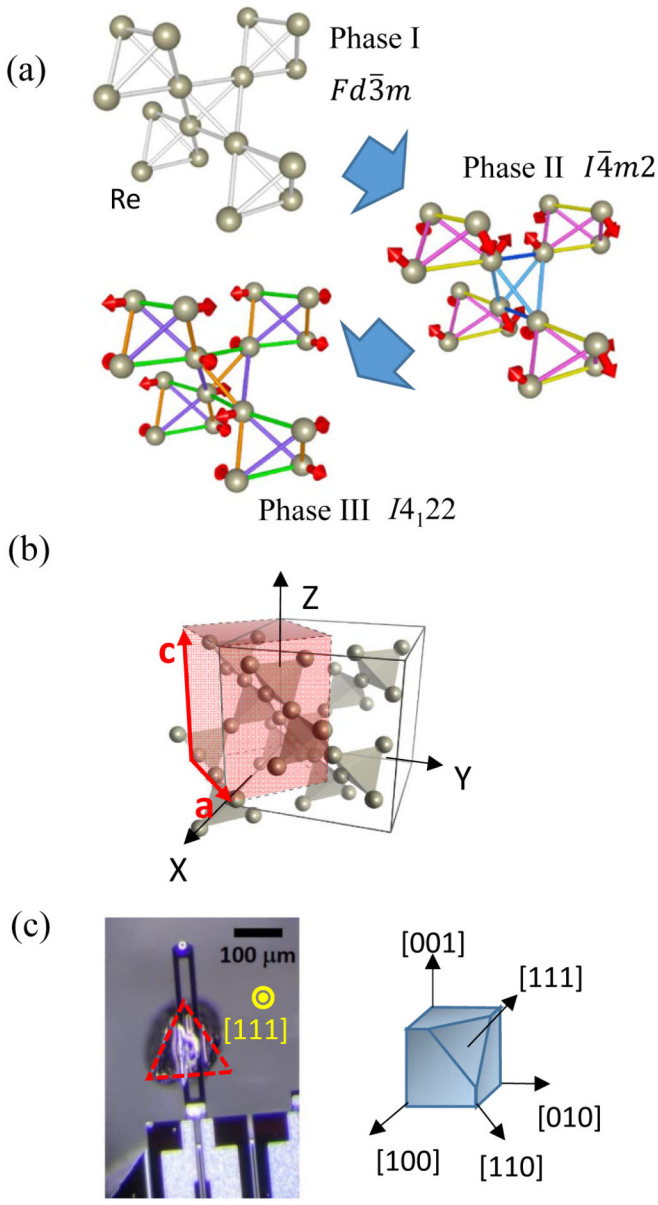

FIG. 1. (a) Crystal structure of $Cd_2Re_2O_7$.Tetrahedra formed by four Re atoms with bonds in three phases I, II, and III. Each bond color indicates the same length and red arrows show the displacements of the Re atoms. In phase I with space group $Fd\bar{3}m$, all the tetrahedra are equivalent but two different tetrahedra are formed in phases II ($I\bar{4}m2$) and III ($I4_122$). (b) Unit cell (red region) in phases II and III. Three c-axis- oriented domains are formed. (c) Photo of the torque magnetometry, where a single crystal is attached on the back of a piezo-microcantilever. The major crystal axes in phase I are also indicated. The crystal axes are aligned along the cantilever within the accuracy of several degrees.

cantilever with silicone grease. The signal V_{AB} is detected by a lock-in amplifier with a frequency of ∼15 Hz, using a homemade bridge circuit. The experiments were performed with a ^{4}He gas flow cryostat and a 15 T superconducting magnet. The cantilever chip is precisely rotated in the cryostat by a stepping motor. The background signal arising from the cantilever bending by the sample gravity is numerically

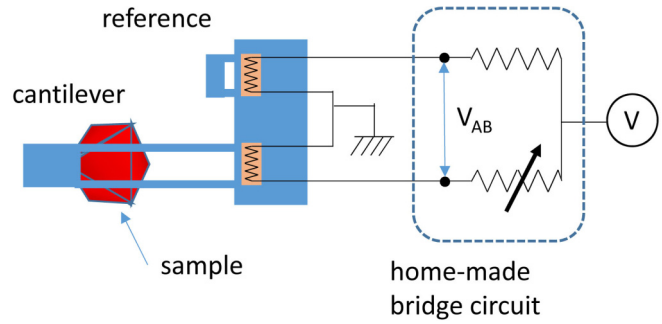

FIG. 2. Schematic of the circuit diagram for torque measurements. The voltage V_{AB}, corresponding to the sample torque, is detected by a lock-in amplifier.

subtracted. This background subtraction can be easily done because of a $\sin(\theta)$ dependence at zero field.

III. RESULTS

The torque curves have been measured in magnetic fields rotated in three different planes; H in (001), (1$\bar{1}$0), and (111) planes in the notation of the phase I structure. Figure 3 presents the torque curves as a function of the field angle

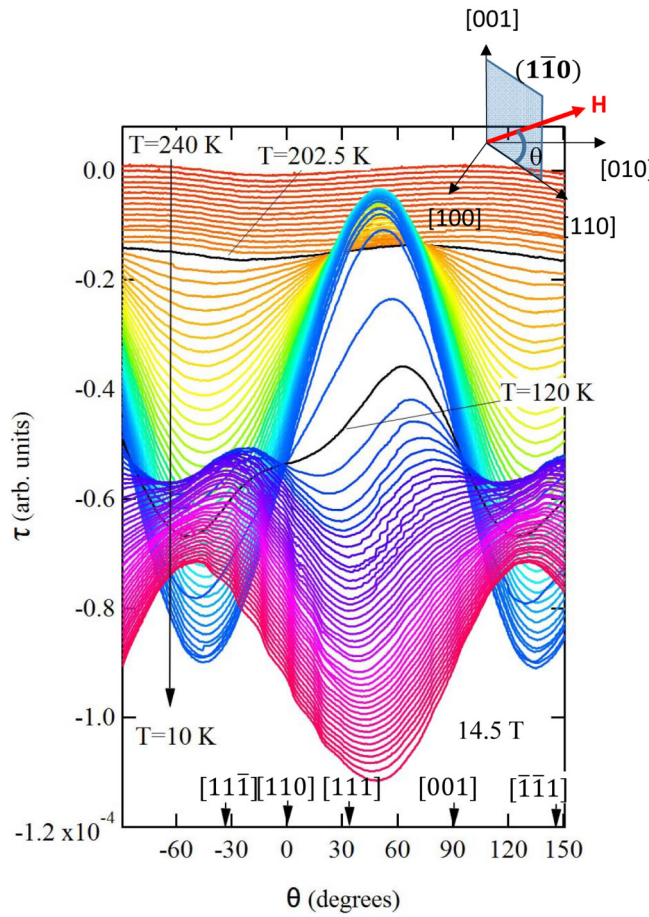

FIG. 3. Torque curves as a function of the field angle θ for H in (1$\bar{1}$0) plane. The data are taken from 250 to 10 K with a step of 2.5 K at 14.5 T. Each curve is shifted for clarity.

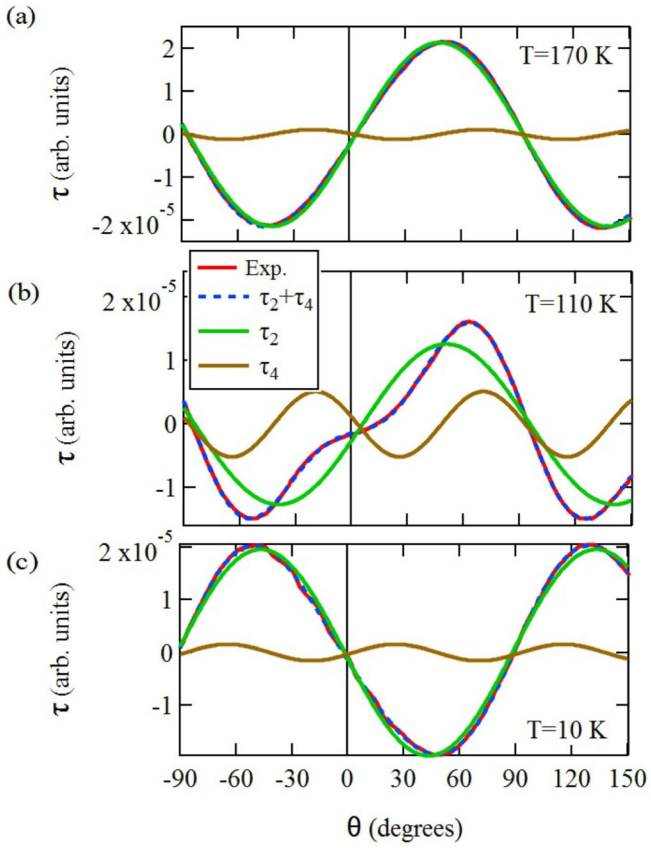

FIG. 4. Torque curves for H in $(1\bar{1}0)$ plane at (a) 170 K, (b) 110 K, and (c) 10 K. Each curve is completely reproduced by the summation of twofold (τ_2) and fourfold (τ_4) terms.

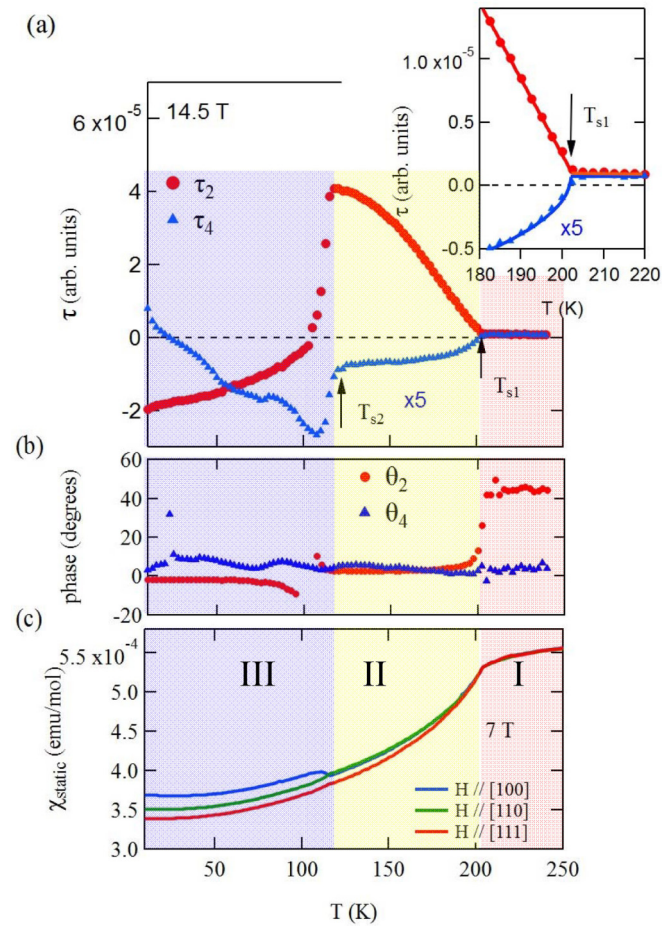

FIG. 5. (a) τ_2 and τ_4, (b) θ_2 and θ_4 obtained by fitting the torque curves with Eq. (1). Inset shows the closeup of τ_2 and τ_4 around T_{s1}. Solid curves indicate $\tau_2 \propto (1 - T/T_{s1})$ and $\tau_4 \propto (1 - T/T_{s1})^{1/2}$ for $T_{s1} = 202$ K. (c) Static magnetic susceptibility χ_{static} measured at 7 T.

θ at various temperatures for H in $(1\bar{1}0)$. Above T_{s1} (phase I), we obtain a small sinusoidal torque signal. Below T_{s1} (phase II), the torque is enhanced and then largely deformed at ~120 K. As temperature further decreases, the torque curve has a strong twofold symmetry but the amplitude is reversed. No significant differences are found between the zero-field- and field-cooling processes. To elucidate the torque curve symmetry, we fit the torque curves with a functional form,

$$\tau(\theta) = \tau_2 \sin[2(\theta - \theta_2)] + \tau_4 \sin[4(\theta - \theta_4)]. \quad (1)$$

All the torque curves are completely reproduced by Eq. (1) as shown in Fig. 4; the curves can be decomposed into twofold $\sin(2\theta)$ and fourfold $\sin(4\theta)$ terms. The obtained amplitudes (τ_2 and τ_4) and phases (θ_2 and θ_4) are presented in Figs. 5(a) and 5(b), respectively. For comparison, the static magnetic susceptibilities (χ_{static}) measured by a conventional superconducting quantum interference device at 7 T are presented in Fig. 5(c).

We obtain small τ_2 and τ_4 values in phase I, which are consistent with very small anisotropy of χ_{static}. Below T_{s1}, the absolute amplitudes of τ_2 and τ_4 steeply increase, suggesting significant changes of the *5d* electronic states. In the inset of Fig. 5(a), the close-up of τ_2 and τ_4 near T_{s1} is presented. The temperature dependence can be fitted with a function $(1 - T/T_{s1})^{\beta}$ below T_{s1}. We obtain β by a least-mean-square fit for all the samples as shown below; $\beta = 1.1 \pm 0.1$ for τ_2 and $\beta = 0.55 \pm 0.07$ for τ_4. The fitting results reasonably lead us to conclude that $\beta = 1$ for τ_2 and $\beta = 0.5$ for τ_4. We note a steep decrease of the phase θ_2 at T_{s1}, which will be discussed later. Below T_{s1}, both the phases θ_2 and θ_4 seem nearly zero. At T_{s2}, we clearly observe steep changes of τ_2 and τ_4, showing a first-order phase transition. The strange behavior of θ_2 at ~105 K arises from an artifact of the curve fitting. The χ_{static} values at all the field directions decrease with decreasing temperature [Fig. 5(c)]. Anisotropic behavior is evident below T_{s1}, consistent with the large changes of τ_2 and τ_4. We see a small jump at T_{s2} for H // [100]. Figure 6 presents the torque curves at various fields for $T = 195$ K (phase II). By fitting the curves with Eq. (1), we obtain the field dependences of τ_2 and τ_4 at 195 and 100 K (phase III). The solid curves indicate H^2 and H^4 dependences, which reasonably reproduce the experimental data of τ_2 and τ_4, respectively.

The torque results for H in (001) at various temperatures are presented in Fig. 7(a). All the curves are also reproduced by Eq. (1). The amplitudes and phases are shown in Figs. 7(b) and 7(c), respectively. Below T_{s1}, both the absolute amplitudes rapidly increase with decreasing temperatures. At around T_{s2}, we see small jumps in τ_2 and τ_4. We note that $\tau_2 \propto (1 - T/T_{s1})$ and $\tau_4 \propto (1 - T/T_{s1})^{1/2}$ below T_{s1}, as shown by

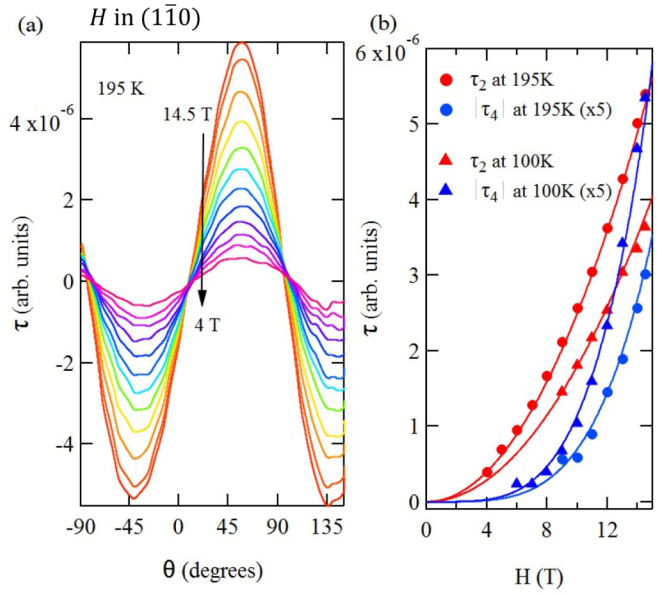

FIG. 6. (a) Torque curves at various fields (4 ∼ 14.5 T) for H in (1$\bar{1}$0) at 195 K. (b) Field dependences of τ_2 and τ_4 at 195 K (phase II) and 100 K (phase III). Solid curves indicate $\tau_2 \propto H^2$ and $\tau_4 \propto H^4$.

solid curves in the inset of Fig. 7(b). The torque curves at various fields for $T = 180$ K (phase II) are presented in Fig. 8. Both τ_2 and τ_4 seem to follow H^2 and H^4 dependences, respectively, as shown by solid curves.

The torque curves for H in (111) are presented in Fig. 9 (a), all of which can also be reproduced by Eq. (1). The results are shown in Figs. 9(b) and 9(c). The τ_2 and τ_4 values are enhanced below T_{s1}, and then jumps are evident at T_{s2}. We see that $\tau_2 \propto (1 - T/T_{s1})$ below T_{s1} [inset of Fig. 9(a)] whereas the behavior of τ_4 is not clear because of the small signal. We see drastic changes of the phases θ_4 at T_{s1} and θ_2 at T_{s2}. Figure 10(a) shows the torque curves at 150 K. We see that the obtained τ_2 and τ_4 in Fig. 10(b) follow H^2 and H^4 dependences, respectively, as shown by solid curves. In this way, we observe very consistent behavior in all the rotations, $\tau_2 \propto (1 - T/T_{s1})$ and $\tau_4 \propto (1 - T/T_{s1})^{1/2}$ below T_{s1}, and $\tau_2 \propto H^2$ and $\tau_4 \propto H^4$ in phase II. The free energy due to the magnetic field, $\sim \chi_{\text{static}} H^2$ is an order of 0.1 K at 15 T, which is much smaller than $k_B T_{s1}$ or the SO coupling strength (∼70 K) [6]. Therefore, the magnetic energy will cause no significant change to the phase transitions.

IV. ANALYSES AND DISCUSSIONS

A. Phase I

In phase I, the free energy F of the electronic state can be expanded into a polynomial of the magnetic field $\boldsymbol{H} = (H_x, H_y, H_z)$, in which each term is classified into the IR Γ of the point group O_h,

$$F(\boldsymbol{H}) = F_0 + \sum_n \sum_\Gamma c_\Gamma^{(n,0)} \chi_\Gamma^{(n)}(\boldsymbol{H}). \quad (2)$$

Here, F_0 is the energy at zero field, $\chi_\Gamma^{(n)}(\boldsymbol{H})$ is a magnetic field function of nth order term of $\boldsymbol{H}$, corresponding to the bases of Γ, and $c_\Gamma^{(n,0)}$ is a coefficient. The magnetization

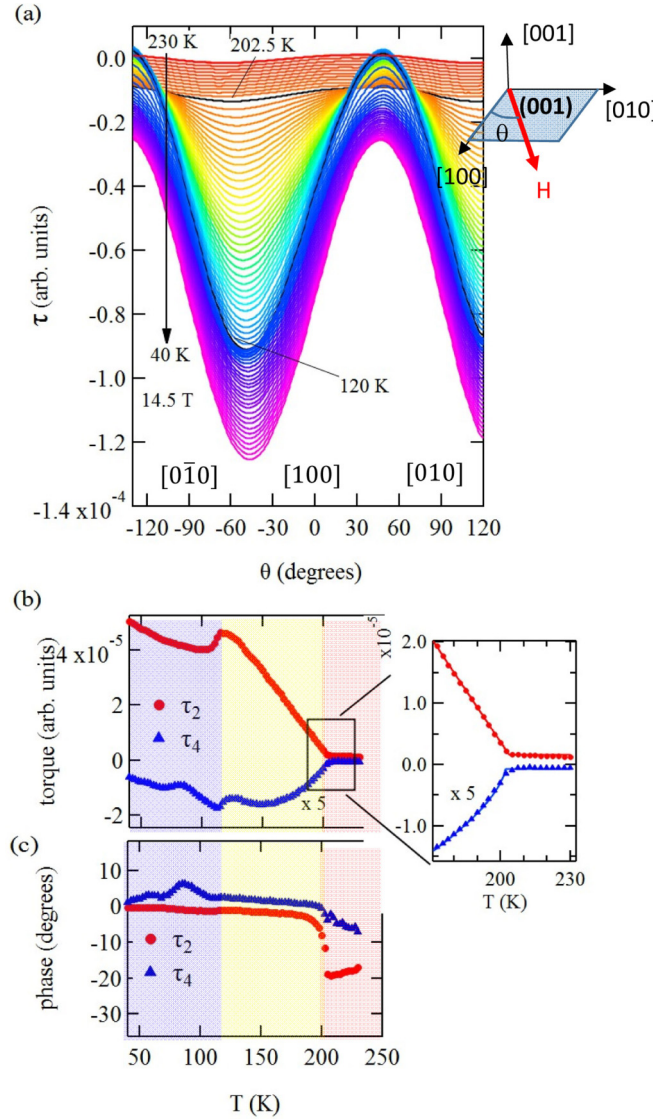

FIG. 7. (a) Torque data at 14.5 T for H in (001) from 230 to 40 K with a step of 2.5 K. Each curve is shifted for clarity. (b) τ_2 and τ_4, (c) θ_2 and θ_4 obtained by fitting the torque curves with Eq. (1). Inset shows the close-up of τ_2 and τ_4 around T_{s1}. Solid curves indicate $\tau_2 \propto (1 - T/T_{s1})$ and $\tau_4 \propto (1 - T/T_{s1})^{1/2}$ for $T_{s1} = 202$ K.

is expressed as $\boldsymbol{M} = -\nabla_H F(\boldsymbol{H})/2$. In the point group O_h, the possible IRs of $\chi_\Gamma^{(n)}(\boldsymbol{H})$ up to the fourth-order of $\boldsymbol{H}$ are listed in Table I. We should note that the even-parity IRs are responsible for $\chi_\Gamma^{(n)}(\boldsymbol{H})$. In phase I, the free energy includes only terms with the totally symmetric IR A_{1g} of O_h. Therefore, the free energy up to the fourth-order terms of $\boldsymbol{H}$ can be

TABLE I. Irreducible representations of the point group O_h responsible for the magnetic field function $\chi_\Gamma^{(n)}(\boldsymbol{H})$.

Order of H	Irreducible representation Γ
H	T_{1g}
H^2	A_{1g}, E_g, T_{2g}
H^3	A_{2g}, $2T_{1g}$, T_{2g}
H^4	$2A_{1g}$, $2E_g$, T_{1g}, $2T_{2g}$

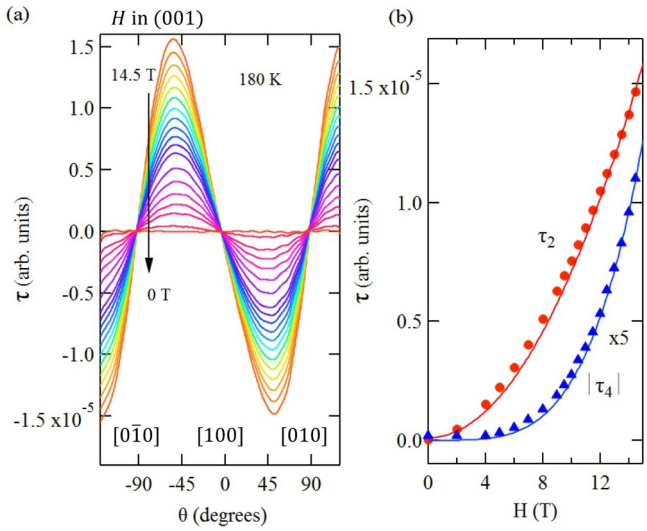

FIG. 8. Torque data for H in (001). (a) Torque curves at various fields (0 ∼ 14.5 T) for H in (001) at 180 K. (b) Field dependences of τ_2 and τ_4 at 180 K (phase II), which are obtained by fitting the torque curves with Eq. (1). Solid curves indicate $\tau_2 \propto H^2$ and $\tau_4 \propto H^4$.

expressed as

$$F = F_0 + c^{(2,0)}_{A_{1g}} \chi^{(2)}_{A_{1g}}(\boldsymbol{H}) + c^{(4,0)}_{A_{1g}(a)} \chi^{(4)}_{A_{1g}(a)}(\boldsymbol{H}) + c^{(4,0)}_{A_{1g}(b)} \chi^{(4)}_{A_{1g}(b)}(\boldsymbol{H}). \tag{3}$$

Note there are two $\chi^{(4)}_{A_{1g}}(\boldsymbol{H})$ functions as seen below. The magnetic torque $\tau(\boldsymbol{H})$ is obtained from the field angle derivative of the free energy,

$$\tau(\boldsymbol{H}) \propto -\frac{\partial F(\boldsymbol{H})}{\partial \theta} = \sum_n \sum_\Gamma c^{(n,0)}_\Gamma \tau^{(n)}_\Gamma(\boldsymbol{H}), \tag{4}$$

where $\tau^{(n)}_\Gamma(\boldsymbol{H}) = -\partial \chi^{(n)}_\Gamma(\boldsymbol{H})/\partial\theta$ and θ is an angle between the magnetic field and a specific axis of the crystal. The field components in three field rotations are defined as

$$H \text{ in } (001) : (H\cos\theta,\ H\sin\theta,\ 0), \tag{5}$$

$$H \text{ in } (1\bar{1}0) : \left(\frac{H\sin\theta}{\sqrt{2}}, \frac{H\sin\theta}{\sqrt{2}}, H\cos\theta\right), \tag{6}$$

$$H \text{ in } (111) : \left(\frac{-\sqrt{3}H\cos\theta - H\sin\theta}{\sqrt{6}}, \right.$$
$$\left. \times \frac{\sqrt{3}H\cos\theta - H\sin\theta}{\sqrt{6}}, \frac{2H\sin\theta}{\sqrt{6}}\right). \tag{7}$$

The second and fourth-order terms of $\chi^{(n)}_\Gamma(\boldsymbol{H})$ are listed in Table II of Appendix A. We have the isotropic free energy terms $\chi^{(2)}_{A_{1g}}(H) = H^2$ and $\chi^{(4)}_{A_{1g(a)}}(H) = H^4$, but the anisotropic one, $\chi^{(4)}_{A_{1g(b)}}(H) = (H_x^2 H_y^2 + H_y^2 H_z^2 + H_z^2 H_x^2)$.

Tables III and IV in Appendix B present the calculated $\tau^{(n)}_\Gamma(\boldsymbol{H})$ with $n = 2$ and 4, respectively, for $\boldsymbol{H}$ in (100), (1$\bar{1}$0), and (111) planes. The resultant torque signals, $\tau^{(2)}_{A_{1g}}(H)$ and $\tau^{(4)}_{A_{1g(a)}}(H)$ vanish for any field rotations but $\tau^{(4)}_{A_{1g(b)}}(H)$ leads to $-(H^4/4)\sin(4\theta)$ for H in (001) and $-(H^4/8)[2\sin(2\theta) + 3\sin(4\theta)]$ for H in (1$\bar{1}$0). The results

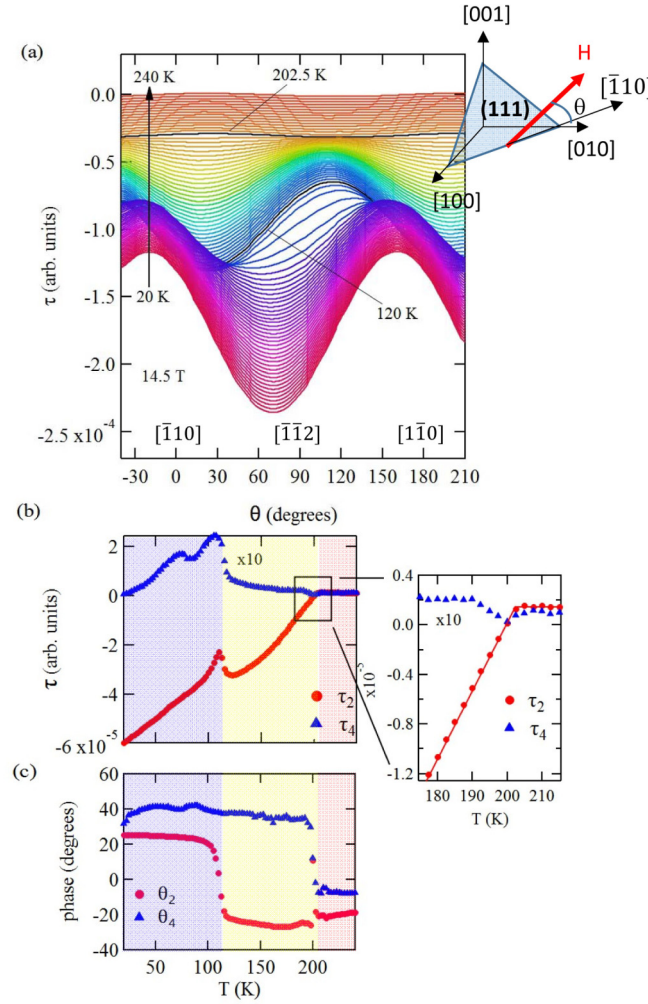

FIG. 9. (a) Torque curves at 14.5 T for H in (111) from 240 to 20 K with a step of 2.5 K. Each curve is shifted for clarity. (b) τ_2 and τ_4, (c) θ_2 and θ_4 obtained by fitting the torque curves with Eq. (1). Inset shows the close-up of τ_2 and τ_4 around T_{s1}. Solid curve indicates $\tau_2 \propto (1 - T/T_{s1})$.

show that τ_2 and τ_4 terms with $\theta_2 = \theta_4 = 0$ could be observed in phase I but are inconsistent with the experimental results. The small torque in phase I may be induced by some local lattice distortion of the crystal or by the anisotropic demagnetization effect. Although the interpretation of the torque curve in phase I is ambiguous, our discussions on the results for $T < T_{s1}$ are not affected.

B. Phase II

In phase II, the symmetry of the electronic state is reduced, associated with the structural transition (point group $O_h \rightarrow D_{2d}$). It is reasonable to analyze the free energy based on Landau theory within a molecular field approximation. According to the Landau theory, we can describe the coupling terms between the OP $\boldsymbol{\eta}$ and $\boldsymbol{H}$ in the free energy as follows, which are sufficient in the discussion of the torque curve symmetry:

$$F = \sum_{m,n,\Gamma} c^{(n,m)}_\Gamma \sum_{i=1}^{d_\Gamma} f^{(m)}_{\Gamma_i}(\boldsymbol{\eta}) \chi^{(n)}_{\Gamma_i}(\boldsymbol{H}). \tag{8}$$

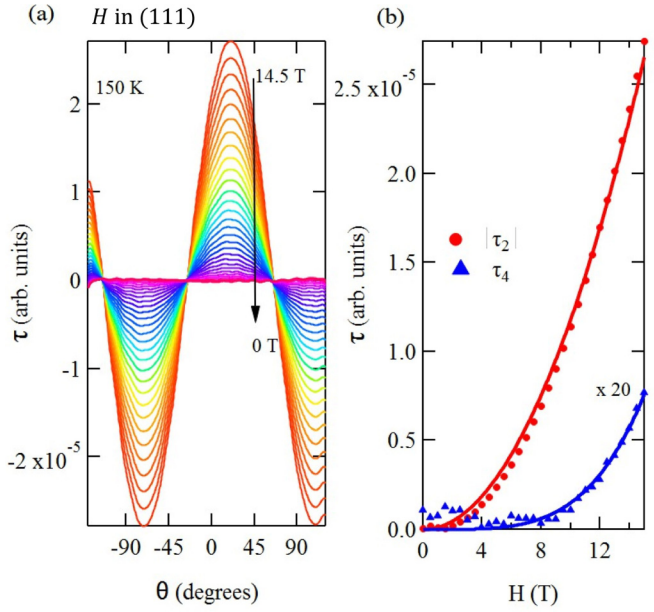

FIG. 10. (a) Torque curves at various fields (0 ∼ 14.5 T) for H in (111) at 150 K. (b) Field dependences of τ_2 and τ_4 at 150 K (phase II), which are obtained by fitting the torque curves with Eq. (1). Solid curves indicate $\tau_2 \propto H^2$ and $\tau_4 \propto H^4$.

Here $c_\Gamma^{(n,m)}$ is a constant, d_Γ is the dimension of an IR Γ of O_h, Γ_i is the ith component of Γ, n is an order of H, and m is an order of $\boldsymbol{\eta}$. The OP function $f_{\Gamma_i}^{(m)}(\boldsymbol{\eta})$ includes mth order terms of $\boldsymbol{\eta}$, classified by Γ_i. Both the functions f_Γ and χ_Γ must have the same IR Γ.

Since we observe only even order terms, $\tau_2 \propto H^2$ and $\tau_4 \propto H^4$, we obtain possible IRs, $\Gamma = A_{1g}$, E_g, T_{1g}, or T_{2g} as listed in Table I. The absence of the odd order terms shows no magnetic order, consistent with the nuclear magnetic resonance (NMR) results [14,15]. Since $\eta \propto (1 - T/T_{s1})^{1/2}$ in the framework of the Landau theory, we expect $\tau_2 \propto \eta_{\tau 2}^2$ and $\tau_4 \propto \eta_{\tau 4}$, where $\eta_{\tau 2}$ and $\eta_{\tau 4}$ are the OPs leading to the twofold and fourfold torque curves, respectively. Consequently, we can conclude that the τ_2 term arises from $f_{\Gamma_i}^{(2)}(\boldsymbol{\eta}_{\tau 2})\chi_{\Gamma_i}^{(2)}(\boldsymbol{H})$, and τ_4 from $f_{\Gamma'_i}^{(1)}(\boldsymbol{\eta}_{\tau 4})\chi_{\Gamma'_i}^{(4)}(\boldsymbol{H})$, where Γ and Γ' could be different.

By comparing the anisotropy of the torque data with the calculated results in Tables III and IV, we can determine Γ of $\chi_\Gamma^{(n)}(\boldsymbol{H})$. First we discuss the torque data for H // (001) in Fig. 7, where we observe $\tau_2 \propto H^2\sin(2\theta)$ and $\tau_4 \propto H^4\sin(4\theta)$ with $\theta_2 \approx 0$ and $\theta_4 \approx 0$ in phase II. For instance, there are a single $\chi_\Gamma^{(2)}(\boldsymbol{H})$ function for $\Gamma = A_{1g}$, $\chi_{A_{1g}}^{(2)}(\boldsymbol{H}) = H^2$, two functions for E_g, $\chi_{E_{g(1)}}^{(2)}(H) = H_x^2 - H_y^2$ and $\chi_{E_{g(2)}}^{(2)}(\boldsymbol{H}) = (H_x^2 + H_y^2 - 2H_z^2)/\sqrt{3}$, and three functions for T_{2g}, $\chi_{T_{2g(1)}}^{(2)}(\boldsymbol{H}) = H_yH_z$, $\chi_{T_{2g(2)}}^{(2)}(\boldsymbol{H}) = H_zH_x$, and $\chi_{T_{2g(3)}}^{(2)}(\boldsymbol{H}) = H_xH_y$ (Table II). There are no $\chi_\Gamma^{(2)}(\boldsymbol{H})$ functions in other IRs. From Table III, we note that only $E_{g(1)}$ gives $\tau_2 \propto H^2\sin(2\theta)$, consistent with the experimental results. Similarly, the $\chi_\Gamma^{(4)}(\boldsymbol{H})$ functions for $\Gamma = A_{1g(b)}$, $E_{g(a)}$, and $E_{g(b)}$ in Table II lead to $\tau_4 \propto H^4\sin(4\theta)$ in Table IV. In this way, we obtain the possible IRs of the OPs: $\Gamma = E_g$ for τ_2, and $\Gamma = A_{1g}$, $E_{g(a)}$, or $E_{g(b)}$ for τ_4. The IRs T_{1g} and T_{2g} are excluded.

For H in $(1\bar{1}0)$, we also observe $\tau_2 \propto H^2\sin(2\theta)$ and $\tau_4 \propto H^4\sin(4\theta)$ in Fig. 5. From Tables III and IV, we consistently obtain that $\Gamma = E_g$ for τ_2, and $A_{1g(b)}$, $E_{g(a)}$, or $E_{g(b)}$ for τ_4. For H in (111), we observe $\tau_2 \propto H^2\sin[2(\theta - \theta_2)]$ and $\tau_4 \propto H^4\sin[4(\theta - \theta_4)]$ with $\theta_2 \approx -20^o$ and $\theta_4 \approx 40^o$ in Fig. 9. In this rotation, arbitrary phases in both τ_2 and τ_4 terms could be observed for $E_{g(a)}$, depending on the domain structures (Appendix C). An important point is that A_{1g} for τ_4 is eliminated because of the observation of the $H^4\sin[4(\theta - \theta_4)]$ term. The result is consistent with the Landau theory since the symmetry is lowered in Phase II. Consequently, we can unambiguously specify the same IR, E_g for both τ_2 and τ_4. Here, we should note that $\tau_{E_g}^{(4)}(\boldsymbol{H})$ has a $H^4\sin(2\theta)$ term in addition to $H^4\sin(4\theta)$ for H in $(1\bar{1}0)$ and (111). The $H^4\sin(2\theta)$ term is not experimentally observable, showing that the $H^2\sin(2\theta)$ term in $\tau_{E_g}^{(2)}(\boldsymbol{H})$ is much larger.

The transition to the tetragonal unit cell at T_{s1} inevitably leads to three c-axis-oriented domains [Fig. 1(b)], which are assigned by the rotation of the OP vectors (Appendix C). Each domain is denoted as $X(c//X)$, $Y(c//Y)$, or $Z(c//Z)$. As shown in Appendix C, the above discussions on Γ are not affected by the domain structures. For instance, we can show that any domain has a same functional form $\tau_2 \propto H^2\sin(2\theta)$ with $\Gamma = E_g$ in $H//(1\bar{1}0)$, which is consistent with the experimental results. When all the domains are equally distributed, the torque signal vanishes for $\Gamma = E_g$. Polarized microscope images show the typical single domain size of ∼0.05 mm, which is comparable to the single crystals used for the torque measurements ($\sim 0.1 \times 0.1 \times 0.1\,\mathrm{mm}^3$). Therefore, we expect an inhomogeneous distribution of the domains, which enables us to detect the torque curves in phases II and III. Actually, we obtain $\theta_2 \approx 0$ and $\theta_4 \approx 0$ for H in (001) and $(1\bar{1}0)$ for different samples although the amplitudes τ_2 and τ_4 are sample dependent. The results clearly show that the assignments of the IRs are not affected by the domain structures. By contrast, both the phases for H in (111) are sample dependent since arbitrary phases are possible, depending on the domain structure.

The torque curve analyses show the presence of two terms in Eq. (8), $f_{Eg}^{(1)}(\boldsymbol{\eta})\chi_{Eg}^{(4)}(\boldsymbol{H})$ giving τ_4 and $f_{Eg}^{(2)}(\boldsymbol{\eta})\chi_{Eg}^{(2)}(\boldsymbol{H})$ giving τ_2. Therefore, we immediately obtain that the former term arises from the even-parity OP η_g, $f_{Eg}^{(1)}(\boldsymbol{\eta}_g) = \eta_g \propto (T_C - T)^{1/2}$. Since the structural change in phase II, $I\bar{4}m2$ is expressed by the OP with E_u, it is likely that the latter term arises from the E_u OP $\boldsymbol{\eta}_u = (h_{u1}, h_{u2})$. Their second-order terms, $2\eta_{u1}\eta_{u2}$ and $(\eta_{u1}^2 - \eta_{u2}^2)$ belong to E_g, as seen in Table VII of Appendix D and then we obtain $f_{Eg}^{(2)}(\eta_{u1}, \eta_{u2}) \propto O(\eta_u^2) \propto (T_C - T)$, consistent with the experimental results. On the other hand, the second-order terms of the OPs $(\eta_{u1}, \eta_{u2}, \eta_{u3})$ with both T_{1u} and T_{2u} can also have the OPs $(\eta_{u1}^2 - \eta_{u2}^2, (\eta_{u1}^2 + \eta_{u2}^2 - 2\eta_{u3}^2)/\sqrt{3})$ belonging to E_g, as shown in Table VIII of Appendix D. These terms can explain the data $f_{Eg}^{(2)} \propto O(\eta_u^2) \propto (T_C - T)$.

For instance, if τ_2 arises from the OP η_g with E_g, we should observe a dominant term $\tau_2 \propto f_{Eg}^{(1)}(\boldsymbol{\eta}_g)\chi_{Eg}^{(2)}(\boldsymbol{H}) \propto H^2(T_C - T)^{1/2}$. However, no observation of the $\tau_2 \propto H^2(T_C - T)^{1/2}$ term excludes $f_{Eg}^{(2)}(\boldsymbol{\eta}_g) \propto O(\eta_g^2)$ as the origin of τ_2. Since no H^3 terms are observed in the whole field and

temperature region, we should note that $\Gamma = A_{2g}$, T_{1g}, and T_{2g} are excluded [see Table I]. This is consistent with the above arguments. In this way, we conclude the presence of two distinct odd- and even-parity OPs, $\boldsymbol{\eta}_u$ and $\boldsymbol{\eta}_g$. The free energy up to H^4 will include more terms,

$$F(H) \propto f_{Eg}^{(2)}(\boldsymbol{\eta}_u)\chi_{Eg}^{(2)}(\boldsymbol{H}) + f_{Eg}^{(2)}(\boldsymbol{\eta}_u)\chi_{Eg}^{(4)}(\boldsymbol{H}) + f_{Eg}^{(1)}(\boldsymbol{\eta}_g)\chi_{Eg}^{(4)}(\boldsymbol{H}) + f_{Eg}^{(2)}(\boldsymbol{\eta}_g)\chi_{Eg}^{(4)}(\boldsymbol{H}). \quad (9)$$

The second and fourth terms are not experimentally observed, suggesting that the first and third terms are predominant. It should be noted that only the coupling terms between the OPs and field are detected in the torque measurements; these terms vanish at zero field. The presence of the $f_{Eg}^{(1)}(\boldsymbol{\eta}_g)\chi_{Eg}^{(4)}(\boldsymbol{H})$ term, whose origin is not clear, is surprising and indicative of a peculiar transition in this SO coupled metal. Since the $f_{Eg}^{(2)}(\boldsymbol{\eta}_u)\chi_{Eg}^{(2)}(\boldsymbol{H})$ and $f_{Eg}^{(1)}(\boldsymbol{\eta}_g)\chi_{Eg}^{(4)}(\boldsymbol{H})$ terms are observed, there will be higher order cross terms of $\boldsymbol{\eta}_u$ and $\boldsymbol{\eta}_g$, $\boldsymbol{\eta}_u^2\boldsymbol{\eta}_g H^2$, $\boldsymbol{\eta}_u^2\boldsymbol{\eta}_g H^4$, $\boldsymbol{\eta}_u^2\boldsymbol{\eta}_g^2 H^2$, … giving different temperature dependences. However, we have not observed such cross terms within our experimental accuracy, suggesting that the cross terms are much smaller.

As shown in Figs. 5 and 7, all the torque curves in phase III below T_{s2} are also reproduced by the τ_2 and τ_4 terms, both of which are assigned as $\Gamma = E_g$. Since the phase transition at T_{s2} is of the first-order, τ_2 and τ_4 could show discontinuous changes, likely associated with sudden changes of the domain structure.

Since the SHG/torque measurements are blind to even-/odd-parity symmetries, both are complementary techniques to each other. The SHG measurements below T_{s1} reveal that the symmetries of the optical responses are explained by a primary OP with T_{2u} and a secondary OP with E_u [4]. Phenomenological Landau free energy analyses suggest that another primary OP with T_{1g} is required although it is not detectable in the SHG measurements. The optical responses χ_E and χ_T, respectively corresponding to E_u and T_{2u}, are given by $\chi_E \propto (1 - T/T_c)$ and $\chi_T \propto (1 - T/T_c)^{1/2}$ below T_{s1}. Interestingly, the critical exponents β for χ_E and χ_T coincide with those of the magnetic responses τ_2 and τ_4, respectively. As mentioned above, the torque data show the presence of two primary OPs with the even-parity E_g, and the odd-parity E_u, T_{1u} or T_{2u}, but clearly denies the OP with T_{1g}. The OPs observed in torque experiments are coupled to magnetic field but the OPs in SHG to electric field, which may be the reason for the inconsistency between the two measurements.

Two possible magnetic orders, magnetic quadrupole order with $E_u{}^-$ and magnetic octupole order with $A_{2g}{}^-$ are theoretically proposed [17], based on the symmetry analysis of the SHG measurements [4]. The $E_u{}^-$ order will lead to internal fields at the Re sites but such evidence has not been obtained in the NMR experiments [14,15]. The $A_{2g}{}^-$ order is excluded by the torque experiments as described above. Therefore, the magnetic multipole orders are very unlikely in $Cd_2Re_2O_7$. More recently, electric multipole orders of the Re tetrahedral unit of $Cd_2Re_2O_7$ in phases II and III are discussed from a symmetry point of view [19,20]. In the presence of time reversal symmetry, the IRs E_u and T_{2u} correspond to an electric toroidal quadrupole order, and T_{1u} to an electric dipole order [20]. The E_g OP is assigned to an electric quadrupole order [20]. The torque measurements clearly show the parity mixing at the phase transition in $Cd_2Re_2O_7$. Although it is likely that the SO coupling plays an essential role in the phase transition as suggested theoretically [16], the parity mixing will not be explained only by the SO coupling. Further investigation is required to clarify the detailed mechanism of the phase transition.

V. CONCLUSIONS

In conclusion, the magnetic torque curves in the SO coupled metal $Cd_2Re_2O_7$ are decomposed into two parts, $\tau_2 \propto H^2\sin[2(\theta - \theta_2)]$ and $\tau_4 \propto H^4\sin[4(\theta - \theta_4)]$, which are given by $\tau_2 \propto (1 - T/T_{s1})$ and $\tau_4 \propto (1 - T/T_{s1})^{1/2}$ below T_{s1}. The symmetry analyses show that the τ_2 and τ_4 terms arise from two OPs with different parities, η_u with E_u, T_{1u} or T_{2u} [$\tau_2 \propto O(\eta_u^2)$] and η_g with E_g ($\tau_4 \propto \eta_g$). The parity mixing shows the presence of the peculiar phase transition in $Cd_2Re_2O_7$, which will not be explained only by the SO coupling. A significant feature is the presence of the first-order term of the OP $\boldsymbol{\eta}_g$, $f_{Eg}^{(1)}(\boldsymbol{\eta}_g)\chi_{Eg}^{(4)}(\boldsymbol{H})$ term in the free energy. Further theoretical investigations will be required to clarify the microscopic mechanism of the phase transition.

ACKNOWLEDGMENTS

We acknowledge valuable discussions with Y. Motome, and S. Hayami. This work was supported by a Grants-in-Aid for Scientific Research from MEXT, Japan [Nos. 17H01144, JP18K13491, and JP18H04308 (J-Physics)].

APPENDIX A: MAGNETIC FIELD FUNCTIONS

The second and fourth-order terms of magnetic field functions $\chi_\Gamma^{(n)}(\boldsymbol{H})$ are listed in Table II. Note that there are two

TABLE II. Magnetic field functions $\chi_\Gamma^{(2)}(H)$ and $\chi_\Gamma^{(4)}(H)$.

Γ	$\chi_\Gamma^{(2)}(H)$	$\chi_\Gamma^{(4)}(H)$
A_{1g}	$\chi_{A_{1g}}^{(2)}(H) = H^2$	$\chi_{A_{1g(a)}}^{(4)}(H) = H^4$
		$\chi_{A_{1g(b)}}^{(4)}(H) = (H_x^2H_y^2 + H_y^2H_z^2 + H_z^2H_x^2)$
E_g	$\chi_{E_{g(1)}}^{(2)}(H) = H_x^2 - H_y^2$	$\chi_{E_{g(a,1)}}^{(4)}(H) = H_z^2(H_x^2 - H_y^2)$
	$\chi_{E_{g(2)}}^{(2)}(H) = \frac{H_x^2+H_y^2-2H_z^2}{\sqrt{3}}$	$\chi_{E_{g(a,2)}}^{(4)}(H) = \frac{2H_x^2H_y^2-H_y^2H_z^2-H_z^2H_x^2}{\sqrt{3}}$
		$\chi_{E_{g(b,1)}}^{(4)}(H) = H_x^4 - H_y^4$
		$\chi_{E_{g(b,2)}}^{(4)}(H) = \frac{H_x^4+H_y^4-2H_z^4}{\sqrt{3}}$
T_{1g}		$\chi_{T_{1g(1)}}^{(4)}(H) = (H_y^2 - H_z^2)H_yH_z$
		$\chi_{T_{1g(2)}}^{(4)}(H) = (H_z^2 - H_x^2)H_zH_x$
		$\chi_{T_{1g(3)}}^{(4)}(H) = (H_x^2 - H_y^2)H_xH_y$
T_{2g}	$\chi_{T_{2g(1)}}^{(2)}(H) = H_yH_z$	$\chi_{T_{2g(a,1)}}^{(4)}(H) = H_x^2H_yH_z$
	$\chi_{T_{2g(2)}}^{(2)}(H) = H_zH_x$	$\chi_{T_{2g(a,2)}}^{(4)}(H) = H_y^2H_zH_x$
	$\chi_{T_{2g(3)}}^{(2)}(H) = H_xH_y$	$\chi_{T_{2g(a,3)}}^{(4)}(H) = H_z^2H_xH_y$
		$\chi_{T_{2g(b,1)}}^{(4)}(H) = (H_y^2 + H_z^2)H_yH_z$
		$\chi_{T_{2g(b,2)}}^{(4)}(H) = (H_z^2 + H_x^2)H_zH_x$
		$\chi_{T_{2g(b,3)}}^{(4)}(H) = (H_x^2 + H_y^2)H_xH_y$

TABLE III. $\tau_\Gamma^{(2)}(H)$ for each IR. $\tau_{\text{obs.}}^{(2)}$ is the observed angle dependence. From the comparison, the IR of $\tau_{\text{obs.}}^{(2)}$ is assigned to E_{g}. For (111), we define two angles, $\theta' = \theta - 120^\circ$, and $\theta'' = \theta + 120^\circ$.

Γ	H in (001)	H in $(1\bar{1}0)$	H in (111)
$A_{1\text{g}}$	0	0	0
$E_{\text{g}(1)}$	$2H^2\sin(2\theta)$	0	$-\frac{2}{\sqrt{3}}H^2\cos(2\theta)$
$E_{\text{g}(2)}$	0	$-\sqrt{3}H^2\sin(2\theta)$	$\frac{2}{\sqrt{3}}H^2\sin(2\theta)$
$T_{2\text{g}(1)}$	0	$-\frac{H^2}{\sqrt{2}}\cos(2\theta)$	$-\frac{2}{3}H^2\sin(2\theta')$
$T_{2\text{g}(2)}$	0	$-\frac{H^2}{\sqrt{2}}\cos(2\theta)$	$-\frac{2}{3}H^2\sin(2\theta'')$
$T_{2\text{g}(3)}$	$-H^2\cos(2\theta)$	$-\frac{1}{2}H^2\sin(2\theta)$	$-\frac{2}{3}H^2\sin(2\theta)$
$\tau_{\text{obs.}}^{(2)}$	$\propto H^2\sin(2\theta)$	$\propto H^2\sin(2\theta)$	$\propto H^2\sin(2\theta+40)$

fourth-order field functions for $\Gamma = A_{1\text{g}}, E_{\text{g}}$ and $T_{2\text{g}}$. The multiple appearance of Γ is classified by a and b. The degenerate components are indexed by 1,2, and 3.

APPENDIX B: TORQUE FUNCTIONS

The second and fourth-order terms of torque functions, $\tau_\Gamma^{(2)}(H)$ and $\tau_\Gamma^{(4)}(H)$ are listed in Tables III and IV, respectively, which are directly compared to the experimental data $\tau_{\text{obs.}}^{(2)}$. The total symmetric IR $A_{1\text{g}}$ gives no second-order torque signal.

APPENDIX C: OP VECTORS AND DOMAIN STRUCTURES

The E_{u} and E_{g} are doubly degenerated (two-dimensional IRs), whose bases are represented as vectors, $\boldsymbol{\eta}_u = (\eta_{u1}, \eta_{u2})$

TABLE IV. $\tau_\Gamma^{(4)}(H)$ for each IR. $\tau_{\text{obs.}}^{(4)}$ is the observed angle dependence. From the comparison, the IR of $\tau_{\text{obs.}}^{(4)}$ is assigned to E_{g}. For (111), we define two angles, $\theta' = \theta - 120^\circ$, and $\theta'' = \theta + 120^\circ$.

Γ	H in (001)	H in $(1\bar{1}0)$	H in (111)
$A_{1\text{g(a)}}$	0	0	0
$A_{1\text{g(b)}}$	$-\frac{H^4}{4}\sin(4\theta)$	$-\frac{H^4}{8}[2\sin(2\theta)+3\sin(4\theta)]$	0
$E_{\text{g(a,1)}}$	0	0	$-\frac{2H^4}{3\sqrt{3}}[\cos(2\theta)-\cos(4\theta)]$
$E_{\text{g(a,2)}}$	$-\frac{H^4}{2\sqrt{3}}\sin(4\theta)$	$-\frac{H^4}{4\sqrt{3}}[2\sin(2\theta)-3\sin(4\theta)]$	$\frac{2H^4}{3\sqrt{3}}[\sin(2\theta)+\sin(4\theta)]$
$E_{\text{g(b,1)}}$	$2H^4\sin(2\theta)$	0	$-\frac{2H^4}{3\sqrt{3}}[2\cos(2\theta)+\cos(4\theta)]$
$E_{\text{g(b,2)}}$	$\frac{H^4}{\sqrt{3}}\sin(4\theta)$	$-\frac{H^4}{4\sqrt{3}}[10\sin(2\theta)+3\sin(4\theta)]$	$\frac{2H^4}{3\sqrt{3}}[2\sin(2\theta)-\sin(4\theta)]$
$T_{1\text{g}(1)}$	0	$\frac{H^4}{2\sqrt{2}}[\cos(2\theta)+3\cos(4\theta)]$	$\frac{H^4}{3\sqrt{3}}[\cos(2\theta')+2\cos(4\theta')]$
$T_{1\text{g}(2)}$	0	$-\frac{H^4}{2\sqrt{2}}[\cos(2\theta)+3\cos(4\theta)]$	$\frac{H^4}{3\sqrt{3}}[\cos(2\theta'')+2\cos(4\theta'')]$
$T_{1\text{g}(3)}$	$-H^4\cos(4\theta)$	0	$\frac{H^4}{3\sqrt{3}}[\cos(2\theta)+2\cos(4\theta)]$
$T_{2\text{g(a,1)}}$	0	$-\frac{H^4}{4\sqrt{2}}[\cos(2\theta)-\cos(4\theta)]$	$-\frac{2H^4}{9}[\sin(2\theta')-2\sin(4\theta')]$
$T_{2\text{g(a,2)}}$	0	$-\frac{H^4}{4\sqrt{2}}[\cos(2\theta)-\cos(4\theta)]$	$-\frac{2H^4}{9}[\sin(2\theta'')-2\sin(4\theta'')]$
$T_{2\text{g(a,3)}}$	0	$-\frac{H^4}{4}\sin(4\theta)$	$-\frac{2H^4}{9}[\sin(2\theta)-2\sin(4\theta)]$
$T_{2\text{g(b,1)}}$	0	$-\frac{H^4}{2\sqrt{2}}[3\cos(2\theta)+\cos(4\theta)]$	$-\frac{H^4}{9}[5\sin(2\theta')+2\sin(4\theta')]$
$T_{2\text{g(b,2)}}$	0	$-\frac{H^4}{2\sqrt{2}}[3\cos(2\theta)+\cos(4\theta)]$	$-\frac{H^4}{9}[5\sin(2\theta'')+2\sin(4\theta'')]$
$T_{2\text{g(b,3)}}$	$-H^4\cos(2\theta)$	$-\frac{H^4}{4}[2\sin(2\theta)-\sin(4\theta)]$	$-\frac{H^4}{9}[5\sin(2\theta)+2\sin(4\theta)]$
$\tau_{\text{obs.}}^{(4)}$	$\propto H^4\sin(4\theta)$	$\propto H^4\sin(4\theta)$	$\propto H^4\sin(4\theta-160)$

TABLE V. Calculated torque curve $\propto f^{(2)}_{E_g}(\boldsymbol{\eta_u})\tau^{(2)}_{E_g}(\boldsymbol{H})$ arising from each domain in phase II with the E_u OP $\boldsymbol{\eta}_u$. Three domains are denoted by $X\,(c//X)$, $Y\,(c//Y)$, and $Z\,(c//Z)$. The common coefficient $C^{(2)}_{E_g}$ is omitted. Here, we define two angles, $\theta' = \theta - 120^\circ$ and $\theta'' = \theta + 120^\circ$

domain	H in (001)	H in $(1\bar{1}0)$	H in (111)
$\boldsymbol{X}$ $(\alpha = -2\pi/3)$	$\eta_u^2 H^2 \sin(2\theta)$	$-\frac{\sqrt{3}}{2}\eta_u^2 H^2 \sin(2\theta)$	$-\frac{2}{\sqrt{3}}\eta_u^2 H^2 \sin(2\theta')$
$\boldsymbol{Y}$ $(\alpha = 2\pi/3)$	$-\eta_u^2 H^2 \sin(2\theta)$	$-\frac{\sqrt{3}}{2}\eta_u^2 H^2 \sin(2\theta)$	$-\frac{2}{\sqrt{3}}\eta_u^2 H^2 \sin(2\theta'')$
$\boldsymbol{Z}$ $(\alpha = 0)$	0	$\sqrt{3}\eta_u^2 H^2 \sin(2\theta)$	$-\frac{2}{\sqrt{3}}\eta_u^2 H^2 \sin(2\theta)$

for E_u, and $\boldsymbol{\eta}_g = (\eta_{g1}, \eta_{g2})$ for E_g. Below T_{s1} (cubic to tetragonal), three domains are formed as shown in Fig. 1(b), which are indicated by $X(c//X)$, $Y(c//Y)$, and$Z(c//Z)$. We define the OPs, $\boldsymbol{\eta}_u = (0, \eta_{u2})$ in the $I\bar{4}m2$ structure (phase II) for $c//Z$ and $\boldsymbol{\eta}_u = (\eta_{u1}, 0)$ in the $I4_122$ structure (phase III) for $c//Z$. When the OP vector $\boldsymbol{\eta}_u$ is redefined as $(\eta_u \sin\alpha, \eta_u \cos\alpha)$, three different domains in phase II can be expressed by the rotation of $\boldsymbol{\eta}$, $\alpha = 0$ or π for $c//Z$,$\alpha = -2\pi/3$ or $\pi/3$ for $c//X$, and $\alpha = 2\pi/3$ or $-\pi/3$ for $c//Y$. We should note that there are two different domains for each c-axis domain (X, Y, or Z) because of the broken inversion symmetry. The additional two domains, which give the same torque curve, are transformed into each other by an inversion symmetry, for instance, $(0, \eta_u)$ and $(0, -\eta_u)$ for $c//Z$. In this expression, the OP functions in Table VII are written as $f^{(2)}_{E_{g(1)}}(\eta_u) = 2\eta_{u1}\eta_{u2} = \eta_u^2 \sin(2\alpha)$ and $f^{(2)}_{E_{g(2)}}(\eta_u) = (\eta_{u1}^2 - \eta_{u2}^2) = -\eta_u^2 \cos(2\alpha)$.

For $H//(1\bar{1}0)$, we obtain the torque curves τ_2 depending on the domain,

$$\begin{aligned}\tau_2 &\propto \sum_{i=1} f^{(2)}_{E_{g_i}}(\boldsymbol{\eta_u})\tau^{(2)}_{E_{g_i}}(\boldsymbol{H}) \\ &= f^{(2)}_{E_{g(1)}}(\eta_u)\tau^{(2)}_{E_{g(1)}}(H) + f^{(2)}_{E_{g(2)}}(\eta_u)\tau^{(2)}_{E_{g(2)}}(H) \\ &= \sqrt{3}\eta_u^2 \cos(2\alpha) H^2 \sin(2\theta).\end{aligned}$$

In any domains (any α values), we note $\tau_2 \propto H^2 \sin(2\theta)$, which is consistent with the experimental results.

The crystals will include all these domains. It should be noted that the torque signal for E_g vanishes if all the domains are equally distributed. The observation of the torque signal clearly shows that the domains are inhomogeneous. This is the case for the other IRs except for A_{1g}. Actually, the signal intensity is different from sample to sample, which is ascribed to the domain structures. As a reference, the angular dependences of the torque curve $\propto f^{(2)}_{E_g}(\boldsymbol{\eta_u})\tau^{(2)}_{E_g}(\boldsymbol{H})$ arising from each domain in phase II are listed in Table V.

For E_g, three domains are similarly defined as the angle β in $\boldsymbol{\eta}_g = (\eta_g \sin\beta, \eta_g \cos\beta)$, $\beta = 0$ for $c//Z$, $\beta = -2\pi/3$ for $c//X$, and $\beta = 2\pi/3$ for $c//Y$. The angular dependences of $\tau^{(4)}(H)$ are shown in Table VI. Here, $f^{(1)}_{E_{g(1)}}(\eta_g) = \eta_g \sin\beta$, and $f^{(1)}_{E_{g(2)}}(\eta_g) = \eta_g \cos\beta$.

The IRs T_{1u} and T_{2u} have triplicate OPs indicated as $(\eta_{u1}, \eta_{u2}, \eta_{u3})$. The OP vector $\boldsymbol{\eta}_u$ is $(0,0, \pm\eta_u)$ for c // Z, $(\pm\eta_u, 0, 0)$ for c // X, or $(0, \pm\eta_u, 0)$ for c // Y. The second-order terms of $\boldsymbol{\eta}_u$ form bases of three different IRs, A_{1g}, E_g, and T_{2g} as shown in Table VIII of Appendix D. Similarly, the E_g bases, $f^{(2)}_{E_{g(1)}}(\eta_u) = \eta_{u1}^2 - \eta_{u2}^2$ and $f^{(2)}_{E_{g(2)}}(\eta_u) = (\eta_{u1}^2 + \eta_{u2}^2 - 2\eta_{u3}^2)/\sqrt{3}$ lead to τ_2 terms given in Table V.

APPENDIX D: OP FUNCTIONS

The second-order OP functions $f^{(2)}_{\Gamma}(\eta_u)$ for the structural OP $\boldsymbol{\eta}_u = (\eta_{u1}, \eta_{u2})$ with E_u are listed in Table VII. Note that their second-order terms, $(2\eta_{u1}\eta_{u2}, \eta_{u1}^2 - \eta_{u2}^2)$ belong to E_g.

TABLE VI. Calculated torque curve $\propto c^{(4)}_{E_g} f^{(1)}_{E_g}(\boldsymbol{\eta_g})\tau^{(4)}_{E_g}(\boldsymbol{H})$ arising from each domain for the E_g OP $\boldsymbol{\eta}_g$. Three domains are denoted by X $(c//X)$, Y $(c//Y)$, and Z $(c//Z)$. Here, we define two angles, $\theta' = \theta - 120^\circ$ and $\theta'' = \theta + 120^\circ$.

domain	H in (001)	H in $(1\bar{1}0)$	H in (111)
$\boldsymbol{X}$	$\frac{\eta_g H^4}{4\sqrt{3}}[12c^{(4)}_{E_{g(b)}} \sin(2\theta) + (c^{(4)}_{E_{g(a)}} - 2c^{(4)}_{E_{g(b)}})\sin(4\theta)]$	$\frac{\eta_g H^4}{8\sqrt{3}}[2(c^{(4)}_{E_{g(a)}} + 5c^{(4)}_{E_{g(b)}})\sin(2\theta) + 3(-c^{(4)}_{E_{g(a)}} + c^{(4)}_{E_{g(b)}})\sin(4\theta)]$	$\frac{2\eta_g H^4}{3\sqrt{3}}[(c^{(4)}_{E_{g(a)}} + 2c^{(4)}_{E_{g(b)}})\sin(2\theta') + (c^{(4)}_{E_{g(a)}} - c^{(4)}_{E_{g(b)}})\sin(4\theta')]$
$\boldsymbol{Y}$	$\frac{\eta_g H^4}{4\sqrt{3}}[-12c^{(4)}_{E_{g(b)}} \sin(2\theta) + (c^{(4)}_{E_{g(a)}} - 2c^{(4)}_{E_{g(b)}})\sin(4\theta)]$	$\frac{\eta_g H^4}{8\sqrt{3}}[2(c^{(4)}_{E_{g(a)}} + 5c^{(4)}_{E_{g(b)}})\sin(2\theta) + 3(-c^{(4)}_{E_{g(a)}} + c^{(4)}_{E_{g(b)}})\sin(4\theta)]$	$\frac{2\eta_g H^4}{3\sqrt{3}}[(c^{(4)}_{E_{g(a)}} + 2c^{(4)}_{E_{g(b)}})\sin(2\theta'') + (c^{(4)}_{E_{g(a)}} - c^{(4)}_{E_{g(b)}})\sin(4\theta'')]$
$\boldsymbol{Z}$	$-\frac{\eta_g H^4}{2\sqrt{3}}(c^{(4)}_{E_{g(a)}} - 2c^{(4)}_{E_{g(b)}})\sin(4\theta)$	$-\frac{\eta_g H^4}{4\sqrt{3}}[2(c^{(4)}_{E_{g(a)}} + 5c^{(4)}_{E_{g(b)}})\sin(2\theta) + 3(-c^{(4)}_{E_{g(a)}} + c^{(4)}_{E_{g(b)}})\sin(4\theta)]$	$\frac{2\eta_g H^4}{3\sqrt{3}}[(c^{(4)}_{E_{g(a)}} + 2c^{(4)}_{E_{g(b)}})\sin(2\theta) + (c^{(4)}_{E_{g(a)}} - c^{(4)}_{E_{g(b)}})\sin(4\theta)]$

TABLE VII. Second-order OP functions $f_\Gamma^{(2)}(\eta_u)$ for E_u. Note $\eta_{u1} = 0$ and $\eta_{u2} \neq 0$ in phase I and $\eta_{u1} \neq 0$ and $\eta_{u2} = 0$ in phase III. See also Appendix C.

Γ	$f_\Gamma^{(2)}(\eta_u)$
A_{1g}	$f_{A_{1g}}^{(2)}(\eta_u) = \eta_{u1}^2 + \eta_{u2}^2$
E_g	$f_{E_{g(1)}}^{(2)}(\eta_u) = 2\eta_{u1}\eta_{u2}$
	$f_{E_{g(2)}}^{(2)}(\eta_u) = \eta_{u1}^2 - \eta_{u2}^2$

TABLE VIII. Possible second-order OP functions $f_\Gamma^{(2)}(\eta_u)$ for OPs $(\eta_{u1},\ \eta_{u2}, \eta_{u3})$ with T_{1u} and T_{2u}.

Γ	$f_\Gamma^{(2)}(\eta_u)$
A_{1g}	$f_{A_{1g}}^{(2)}(\eta_u) = \eta_{u1}^2 + \eta_{u2}^2 + \eta_{u3}^2$
E_g	$f_{E_{g(1)}}^{(2)}(\eta_u) = \eta_{u1}^2 - \eta_{u2}^2$
	$f_{E_{g(2)}}^{(2)}(\eta_u) = (\eta_{u1}^2 + \eta_{u2}^2 - 2\eta_{u3}^2)/\sqrt{3}$
T_{2g}	$f_{T_{2g(1)}}^{(2)}(\eta_u) = \eta_{2u}\eta_{3u}$
	$f_{T_{2g(2)}}^{(2)}(\eta_u) = \eta_{3u}\eta_{1u}$
	$f_{T_{2g(3)}}^{(2)}(\eta_u) = \eta_{1u}\eta_{2u}$

The OP functions $f_\Gamma^{(2)}(\eta_u)$ for the OP $\boldsymbol{\eta}_u = (\eta_{u1}, \eta_{u2},\ \eta_{u3})$ with T_{1u} and T_{2u} are listed in Table VIII. Note that their second-order terms, $(\eta_{u1}^2 - \eta_{u2}^2,\ (\eta_{u1}^2 + \eta_{u2}^2 - 2\eta_{u3}^2)/\sqrt{3})$ belong to E_g.

[1] J. Yamaura and Z. Hiroi, J. Phys. Soc. Jpn. **71**, 2598 (2002).
[2] J. P. Castellan, B. D. Gaulin, J. van Duijn, M. J. Lewis, M. D. Lumsden, R. Jin, J. He, S. E. Nagler, and D. Mandrus, Phys. Rev. B **66**, 134528 (2002).
[3] J. C. Petersen, M. D. Caswell, J. Steven Dodge, I. A. Sergienko, J. He, R. Jin, and D. Mandrus, Nat. Phys. **2**, 605 (2006).
[4] J. W. Harter, Z. Y. Zhao, J.-Q. Yan, D. G. Mandrus, and D. Hsieh, Science **356**, 295, (2017).
[5] Z. Hiroi, J. Yamaura, T. C. Kobayashi, Y. Matsubayashi, and D. Hirai, J. Phys. Soc. Jpn. **87**, 024702 (2018).
[6] Y. Matsubayashi, K. Sugii, H. T. Hirose, D. Hirai, S. Sugiura, T. Terashima, S. Uji, and Z. Hiroi, J. Phys. Soc. Jpn. **87**, 053702 (2018).
[7] C. A. Kendziora, I. A. Sergienko, R. Jin, J. He, V. Keppens, B. C. Sales, and D. Mandrus, Phys. Rev. Lett. **95**, 125503 (2005).
[8] I. A. Sergienko and S. H. Curnoe, J. Phys. Soc. Jpn. **72**, 1607 (2003).
[9] I. A. Sergienko, V. Keppens, M. McGuire, R. Jin, J. He, S. H. Curnoe, B. C. Sales, P. Blaha, D. J. Singh, K. Schwarz, and D. Mandrus, Phys. Rev. Lett. **92**, 065501 (2004).
[10] Y. Ishibashi and M. Iwata, J. Phys. Soc. Jpn. **79**, 044604 (2010).
[11] H. Sakai, H. Kato, S. Kambe, R. E. Walstedt, H. Ohno, M. Kato, K. Yoshimura, and H. Matsuhata, Phys. Rev. B **66**, 100509(R) (2002).
[12] R Jin, J He, J. R. Thompson, M. F. Chisholm, B. C. Sales, and D. Mandrus, J. Phys.: Condens. Matter **14**, L117 (2002).
[13] Z. Hiroi, M. Hanawa, Y. Muraoka, and H. Harima, J. Phys. Soc. Jpn. **72**, 21 (2003).
[14] O. Vyaselev, K. Arai, K. Kobayashi, J. Yamazaki, K. Kodama, M. Takigawa, M. Hanawa, and Z. Hiroi, Phys. Rev. Lett. **89**, 017001 (2002).
[15] K. Arai, K. Kobayashi, K. Kodama, O. Vyaselev, M Takigawa, M. Hanawaa, and Z. Hiroi, J. Phys.: Condens. Matter **14**, L461 (2002).
[16] L. Fu, Phys. Rev. Lett. **115**, 026401 (2015).
[17] S. Di Matteo and M. R. Norman, Phys. Rev. B **96**, 115156 (2017).
[18] C. Rossel, P. Bauer, D. Zech, J. Hofer, M. Willemin, and H. Keller, J. Appl. Phys. **79**, 8166 (1996).
[19] S. Hayami, Y. Yanagi, H. Kusunose, and Y. Motome, Phys. Rev. Lett. **122**, 147602 (2019).
[20] S. Hayami, M. Yatsushiro, Y. Yanagi, and H. Kusunose, Phys. Rev. B **98**, 165110 (2018).